SPECIAL ISSUE ARTICLE

Computational Modeling of Braided Stent Deployment for Interpreting the Mechanism of Stent Flattening

Shunya Shiozaki[1] | Tomohiro Otani[1] | Soichiro Fujimura[2,3] | Hiroyuki Takao[2,3,4] | Shigeo Wada[1]

[1]Department of Mechanical Science and Bioengineering, Graduate School of Engineering Science, Osaka University, Toyonaka, Osaka, 560-8531, Japan

[2]Department of Innovation for Medical Information Technology, The Jikei University School of Medicine, Minato-ku, Tokyo, 105-8471, Japan

[3]Graduate School of Mechanical Engineering, Tokyo University of Science, Katsushika-ku, Tokyo, 125-8585, Japan

[4]Department of Neurosurgery, The Jikei University School of Medicine, Minato-ku, Tokyo, 105-8471, Japan

Correspondence
Tomohiro Otani PhD, Department of Mechanical Science and Bioengineering, Graduate School of Engineering Science, Osaka University, Toyonaka, Osaka, 560-8531, Japan
Email: otani@me.es.osaka-u.ac.jp

Funding information
JSPS Grants-in-Aid for Early-Career Scientists (18H18367); MEXT as "Priority Issue on Post-K computer(Supercomputer Fugaku)" (Integrated Computational Life Science to Support Personalized and Preventive Medicine)(hp190187)

This study develops a computational model of the braided stent for interpreting the mechanism of stent flattening during deployment into curved arteries. Stent wires are expressed using Kirchhoff's rod theory and their mechanical behavior is treated using a corotational beam formulation. The equation of motion of the braided stent is solved in a step-by-step manner using the resultant elastic force and mechanical interactions of wires with friction. Examples of braided stent deployment into idealized arteries with various curvatures are numerically simulated. In cases of low curvature, the braided stent expands from a catheter by releasing the bending energy stored in stent wires, while incomplete expansion is found at both stent ends (i.e., the fish-mouth phenomenon), where relatively little bending energy is stored. In cases of high curvature, much torsional energy is stored in stent wires locally in the midsection of the curvature and the bending energy for stent self-expansion is not fully released even after deployment, leading to stent flattening. These findings suggest that the mechanical state of the braided stent and its transition during deployment play an important role in the underlying mechanism of stent

Abbreviations: 3-D, three dimensional; DOF, degree of freedom; SDF, signed distance function.

flattening.

KEYWORDS
Braided stent, Kirchhoff's rod theory, Corotational beam element, Contact, stent flattening

1 | INTRODUCTION

The braided stent is a self-expanding endovascular device commonly used in the treatment of cerebral aneurysms. It is deployed into cerebral arteries via a catheter with the assistance of guidewires and is expected, as a vascular reconstruction device stent, to assist endovascular coiling by preventing coil protrusion from aneurysms [1, 2] and, as a flow-diverter stent, to isolate the aneurysm from parent arteries [3, 4, 5]. Comparing with the conventional laser-cut stent, which is commonly used in the treatment of vascular stenosis to restore blood flow, the braided stent comprises woven metal wires and thus has relatively high flexibility and low porosity. Owing to these geometric and mechanical properties, the braided stent is suitable for deployment into narrow and curved arteries with aneurysms.

However, technical difficulties in deploying the braided stent are commonly known [6] and lead to inappropriate stent expansion inside the artery. Various types of inappropriate stent expansion are insufficient stent apposition (i.e., stent malapposition), stent underexpansion, ovalization, and flattening; c.f., [7, 8]. In particular, deployment into a highly curved or tortuous artery is considered difficult and several studies noted that an inappropriate stent shape forms in such cases [9, 10, 11]. Ebrahimi et al. [9] mentioned two problems relating to the deployment of the braided stent, namely inward crippling of the distal end of the stent, also called the fish-mouth phenomenon, and a tendency toward flattening at the midsection of the stent in highly curved arteries. These inappropriate stent expansions are critical issues in the treatment of braided stent deployment for physicians, and yet the underlying mechanism remains an open question.

Mechanical behaviors of the braided stent are determined by many physical factors, such as the mechanical properties and shape of the wires and interactions between the wires themselves and the arterial and catheter walls. Although several experimental studies reported the effects of the wire density and braided angle of the braided stent on apparent mechanical characteristics [12, 13], detailed experimental investigation of the mechanical behavior of the braided stent is challenging. To remedy this issue, theoretical models of the braided stent have been proposed for estimating the radial forces of the braided stent for self-expansion, in which the braided stent is modeled as an assembly of single helical springs [14, 15, 16, 17]. Numerical experiments using mechanically consistent computational models are also expected to be an effective alternative and several studies have attempted quantitative estimation of apparent mechanical characteristics of the braided stent [18, 19, 20, 21, 22, 23, 24, 25, 26, 27, 28, 29]. These numerical experiments considered material nonlinearities of stent wires (i.e., superelasticity [18, 20, 21] and viscoelasticity [24]), three-dimensional (3-D) mechanics within the wire cross-sections through discretization of 3-D volume meshes [21], and structural design of the braided stent [19, 22, 23, 25] and performed quantitative validations by conducting experiments and assessments of the stent mechanical characteristics. However, existing computational evaluations mainly focused on basic apparent characteristics of the braided stent, such as the radial stiffness[18, 19, 28, 25], apparent axial rigidity [21, 22, 24], and flexural rigidity [18, 22, 23] because the models have a high computational cost. Hence, underlying mechanisms of inadequate stent expansion, such as stent flattening and the fish-mouth phenomenon, are still poorly understood. A computational model of the braided stent, which allows the expression of mechanical behaviors with reasonable simplification, may overcome this issue and may help improve our knowledge of these underlying mechanisms.

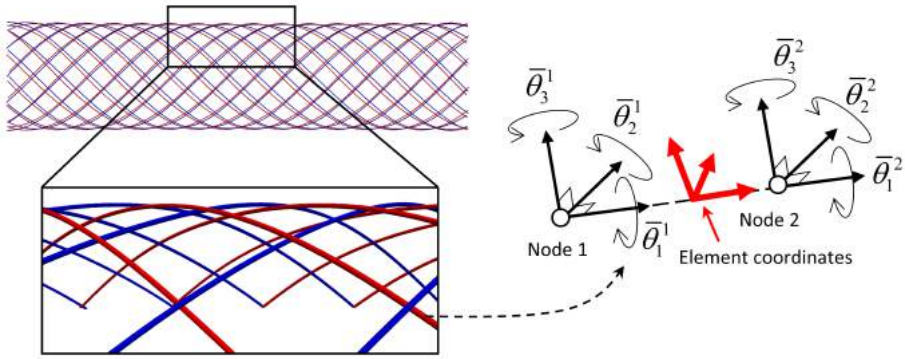

FIGURE 1 Schematic of the computational model of the braided stent. The braided stent is expressed by woven mesh wires that are discretized as sets of two-node beam elements. An orthonormal triad is set for each node, and a node thus has 3-D translational and rotational DOFs.

The present study develops a computational model of the braided stent to deepen our understanding of the underlying mechanism of inadequate stent expansion, especially the stent flattening phenomenon, during deployment into arteries. Section 2 shows the stent modeling strategies and calculation conditions of numerical experiments of braided-stent deployment. Section 3 represents the results of numerical experiments and section 4 discusses the implications and limitations of the study. A brief conclusion is given in section 5.

2 | METHODS

2.1 | Stent modeling

We model the braided stent as an assembly of thin slender wires with closed circular cross-sections (Fig. 1). Stent wire mechanics are expressed using Kirchhoff's rod theory (c.f., [30, 31]) and discretized adopting the corotational beam element formulation [32, 33] to treat geometrical nonlinearity of stent wire behaviors including large deflection. An orthonormal triad of unit vectors is assigned to each node to express the three-dimensional (3-D) rotational degree of freedom (DOF) and a 3-D translational DOF, and each stent node thus has six DOFs. Wires are assembled as a woven mesh with constant braided angle and deformations are calculated by solving the equation of motion while considering frictional contact between wires and arterial and catheter walls.

2.1.1 | Derivation of the internal force of stent wires

The elastic energy of the wire per unit length U is derived by integrating the axial stretching/compression, bending, and torsional elastic energies:

$$U = \frac{1}{2}\left[k_s\varepsilon^2 + k_t\left(\kappa_1 - \kappa_1^0\right)^2 + k_b\left(\kappa_2 - \kappa_2^0\right)^2 + k_b\left(\kappa_3 - \kappa_3^0\right)^2\right], \tag{1}$$

where k_s, k_t, and k_b are respectively the axial, torsional, and flexural rigidities, ε is the axial strain, κ_1, κ_2, and κ_3 are the degrees of twist and curvature, which are components of the Darboux vector $\boldsymbol{\kappa}$, while κ_1^0, κ_2^0, and κ_3^0 are those

in the reference state. In cases that the wire is modeled to be an isotropic linear elastic material, the parameter set (k_s, k_t, k_b) corresponds to (EA, GJ, EI), for Young's modulus E, shear modulus G, cross-section area A, second moment of inertia of area I, and polar moment of inertia of area J of the wire. Using variational calculus, the stress resultants of the wire can be defined from eq. 1 as

$$\mathbf{f}_{\text{int}} = \left[\frac{\partial U}{\partial \boldsymbol{\varepsilon}}, \frac{\partial U}{\partial \boldsymbol{\kappa}} \right] = [n, \mathbf{m}] \in \mathbb{R}^4. \tag{2}$$

Here,

$$n = k_s \varepsilon, \quad m_1 = k_t(\kappa_1 - \kappa_1^0), \quad m_2 = k_b(\kappa_2 - \kappa_2^0), \quad m_3 = k_b(\kappa_3 - \kappa_3^0), \tag{3}$$

where n is the axial force and $\mathbf{m}$ is the moment vector, in which m_1 is the torque and m_2 and m_3 are bending moments.

Stent wires are discretized to be sets of two-node beam elements with 12 DOFs, where the displacement vectors of node p, $\mathbf{U}^p$, have six DOFs as $\mathbf{U}^p = (\mathbf{u}^p, \boldsymbol{\theta}^p)$, where $\mathbf{u}^p \in \mathbb{R}^3$ is the translational displacement and $\boldsymbol{\theta}^p \in \mathbb{R}^3$ is the rotational displacement (Fig. 1(right)). An element coordinate system is assigned on each element, and stress resultants of the beam element (eq. 2) can then be directly discretized in this element coordinate system, $\mathbf{f}_{\text{int,e}} = [n, \mathbf{m}^1, \mathbf{m}^2] \in \mathbb{R}^7$, where $\mathbf{m}^p$ is the moment of the beam node $p = 1, 2$. Note that linear interpolation is used for the axial force and torque and cubic Hermite interpolation is used for the bending moment.

The resultant forces in the global coordinate system are derived using the corotational beam element formulation proposed in [32, 33], such that $\mathbf{f}_{\text{int,g}} = [\mathbf{f}_{\text{g}}^1, \mathbf{m}_{\text{g}}^1, \mathbf{f}_{\text{g}}^2, \mathbf{m}_{\text{g}}^2] \in \mathbb{R}^{12}$, where $\mathbf{f}_{\text{g}}^p$ and $\mathbf{m}_{\text{g}}^p$ are respectively the translational and rotational resultants of the beam node $p = 1, 2$. Coordinate transformation of the stress resultants from the element coordinates $\mathbf{f}_{\text{int,e}}$ to the global coordinates $\mathbf{f}_{\text{int,g}}$ is carried out by introducing the coordinate transformation matrix $\mathbf{B} \in \mathbb{R}^{12\times 7}$ [32, 33], given by

$$\mathbf{f}_{\text{int,g}} = \mathbf{B}\mathbf{f}_{\text{int,e}}. \tag{4}$$

We verified our implementations in a previous study [34].

2.1.2 | Derivation of the repulsive force by frictional contacts

Wire–wire contact, wire–arterial wall contact, and wire–catheter wall contact are detected and contact forces are treated considering friction as in our previous study [34]. A linear viscoelastic model is applied to represent the repulsive force in the normal direction and Coulomb's friction model is used to express the friction force. The arterial wall and catheter are assumed to be rigid for simplicity.

To represent the geometric constraints due to the existence of walls efficiently in computation, we implicitly represented the wall geometry to project into a Cartesian gerid using the sigind distance function (SDF), as shown in Fig. 2). The SDF ψ at each point of the Cartesian grid $\mathbf{x}_{\text{grid}}$ is given by

$$\psi(\mathbf{x}_{\text{grid}}) = \begin{cases} \min \|\mathbf{x}_{\text{grid}} - \mathbf{x}_{\text{wall}}\| & \text{in } \Omega_{\text{in}} \\ 0 & \text{on } \Gamma, \mathbf{x}_{\text{wall}} \in \Gamma \\ -\min \|\mathbf{x}_{\text{grid}} - \mathbf{x}_{\text{wall}}\| & \text{in } \Omega_{\text{out}} \end{cases} \tag{5}$$

where Ω_{in} and Ω_{out} are the domains inside and outside of the wall and Γ is the wall surface (i.e., the interface between Ω_{in} and Ω_{out}). To detect wire–wall contact, the shortest distance between the wire and wall is calculated by linear interpolation of the SDF, where the wire node is located, using the linear shape function of an eight-node hexahedral element [35]. Additionally, the normal-direction vector is calculated through the linear interpolation of spatial derivatives of the SDF. To detect wire–wire contact, a candidate pair of contacting beam elements is searched for by the binning algorithm as introduced in [36] and its shortest distance and normal direction are calculated adopting the methods of [37].

In the event of both wire–wall contact and wire–wire contact, the repulsive force vector in the normal direction $\mathbf{f}_{\text{n}}$ is treated using the linear viscoelastic model, expressed as

$$\mathbf{f}_{\text{n}} = -f_{\text{n}}\mathbf{n} - \eta_{\text{n}} v_{\text{n}} \mathbf{n}, \tag{6}$$

where f_{n} is the elastic force, η_{n} is the viscosity coefficient, and v_{n} is the relative velocity in the normal direction between contacting objects. The repulsive force f_{n} is expressed by $f_{\text{n}} = k_{\text{n}}\delta$, where k_{n} is the elastic coefficient and δ is the indentation depth of the contact. The viscosity coefficient η_n is modeled as the linear damping presented in [38] using the coefficient of restitution e.

The tangential friction force $\mathbf{f}_{\text{t}}$ is expressed using the Coulomb friction model considering slip–stick behavior and adopting the method of [39]. Assuming that the friction force is applied to the translational DOF, the slip friction force is given by

$$\mathbf{f}_{\text{t}} = -\mu_{\text{slip}} f_{\text{n}} \frac{\mathbf{v}_{\text{t}}}{\|\mathbf{v}_{\text{t}}\| + \epsilon_{\text{t}}}, \tag{7}$$

where μ_{slip} is the slip friction coefficient, $\mathbf{v}_{\text{t}}$ is the relative velocity in the tangential direction and ϵ_{t} is a parameter used to avoid division by zero. There is stick friction when the stick friction force is weaker than the maximum stick friction force $\|\mathbf{f}_{\text{t}}\| \leq \mu_{\text{stick}} f_{\text{n}}$, where μ_{stick} is the stick friction coefficient. In this case, the stick friction force is modeled using a linear viscoelastic model, given by

$$\mathbf{f}_{\text{t}} = -k_{\text{t}}\delta_{\text{t}} \frac{\mathbf{v}_{\text{t}}}{\|\mathbf{v}_{\text{t}}\| + \epsilon_{\text{t}}} - \eta_{\text{t}}\mathbf{v}_{\text{t}}, \tag{8}$$

where k_{t} and η_{t} are respectively the linear elastic and viscosity coefficients. These values are set at $k_{\text{t}} = k_{\text{n}}$ and $\eta_{\text{t}} = \eta_{\text{n}}$ following the idea of [40]. The tangential sliding distance δ_{t} is expressed by integrating the total moving distance during contact, given by $\delta_{\text{t}} = \int v_{\text{t}} dt$.

In cases of wire–wall contact, repulsive forces in the normal direction $\mathbf{f}_{\text{n}}$ and tangential direction $\mathbf{f}_{\text{t}}$ are directly assigned on the wire node. Meanwhile, these force vectors are originally defined at each beam element in the wire–wire contact and then linearly interpolated to the wire nodes constituting each beam element.

2.1.3 | Equation of motion

Using the resultant elastic force of the wires and repulsive forces derived in Sections 2.1.1 and 2.1.2, the motion of the braided stent comprising N nodes is expressed by solving the equation of motion in algebraic form, given by

$$\mathbf{M}\mathbf{U} + \mathbf{C}\mathbf{U} + \mathbf{F}_{\text{int}}(\mathbf{U}) = \mathbf{F}_{\text{ext}}(\mathbf{U}), \tag{9}$$

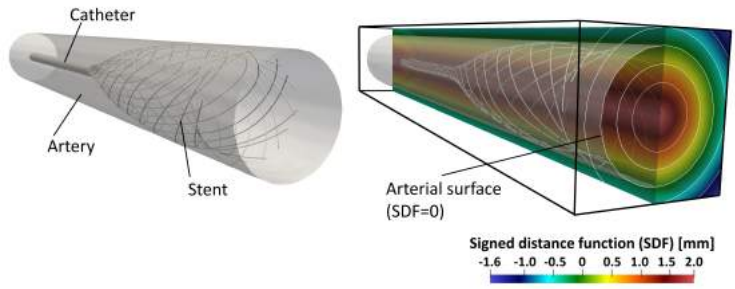

FIGURE 2 Schematics of stent deployment into the artery (left) and signed distance function (SDF) expressing wall surface (SDF=0) in the Cartesian-grid (right).

where $\mathbf{M} \in \mathbb{R}^{6N\times 6N}$ is the mass matrix, $\mathbf{C} \in \mathbb{R}^{6N\times 6N}$ is the damping matrix calculated using the Rayleigh ansatz ($\mathbf{C} = \psi\mathbf{M}$), $\mathbf{F}_{\text{int}} \in \mathbb{R}^{6N}$ is the internal force calculated using the stress resultants $\mathbf{f}_{\text{int,g}}$, $\mathbf{F}_{\text{ext}} \in \mathbb{R}^{6N}$ is the repulsive force due to contacts $\mathbf{f}_n$ and $\mathbf{f}_t$, and $\mathbf{U} \in \mathbb{R}^{6N}$ is the displacement vector of stent nodes including translational and rotational displacements. A dot indicates a derivative with respect to time. We simplify the mass matrix as a diagonal matrix at each wire node p, given by $M^p = \text{diag}[m^p, m^p, m^p, J^p, J^p, J^p]$, where m^p is the mass calculated through linear interpolation for each beam element using the density ρ while J^p is the inertia moment simplified as the values of an isotropic sphere as in [41], because the inertia effect may be insufficient for stent deployment in a quasi-static manner . Equation 9 is solved employing an explicit predictor–corrector scheme with adaptive time stepping proposed by [42, 43] and summarized in [41].

2.2 | Numerical Simulation

A braided stent with an outer diameter of 5 mm and total length of 22.7 mm is constructed. The stent comprises 24 wires (i.e., 12 clockwise/counterclockwise wound wires are braided once every two steps) with a diameter of 0.04 mm. The wire shape in the reference state is set to a single constant helical shape with a braided angle of 45 degrees. Wires are modeled to be made from Co-Cr alloy (E = 225 GPa, G = 98 GPa, $\rho = 9.13 \times 10^3$ kg/m^3). The viscosity coefficient ψ is set to 100 s^{-1} for numerical stability. Wires are discretized by sets of two–node beam elements with an initial length of 0.15 mm. Each wire comprises 198 beam elements. Preliminary analysis of the mesh size sensitivity for the solutions was conducted and confirmed that the mesh size adopted in this study is acceptable in evaluating the mechanical response of the braided stent presented in the results section.

For parameters about contact mechanics, the contact elastic coefficient k_{n} is set at $1\%k_{\text{s}}$, the coefficient of restitution e is set at 0.1, and the stick friction coefficient μ_{stick} of wire–wire contact is set at 0.8 to satisfy the geometric characteristics of stent wires observed in our preliminary experiment. Effects of the frictional coefficient are noted in the discussion section. The stick friction coefficients μ_{stick} of wire–arterial wall contact and wire–catheter contact are respectively set at 0.1 and 0.01 to reduce effects on the numerical solution. The slip friction coefficient is set at $\mu_{\text{slip}} = 0.9\mu_{\text{stick}}$ in each contact for simplicity.

We constructed seven cases of idealized arteries with different curvatures ranging from 0 to 0.094 mm^{-1}. The arterial shape comprises smoothly connected curved and straight domains with a diameter of 4 mm. The arterial centerline is set in the x–z coordinate system on a two-dimensional plane and the center point of the arterial curve is set at the origin. The centerline length of the curved domain is 22 mm in all cases regardless of the curvature. Note

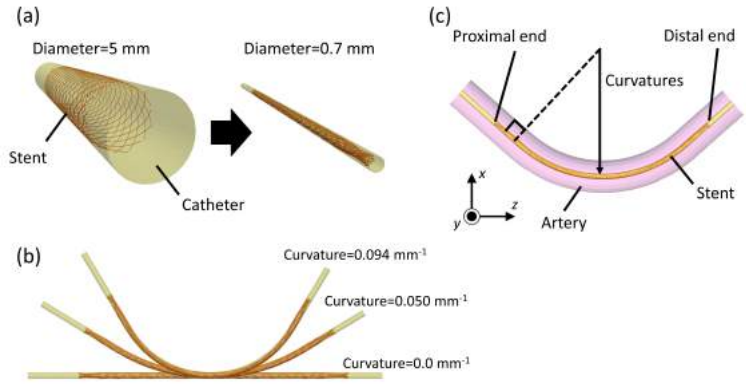

FIGURE 3 Procedure of deploying a braided stent into arteries. The braided stent is set into the catheter and compressed in the radial direction (a) and deformed to fit the centerline of the arteries (b). The braided stent is deployed by pulling the catheter from the distal to the proximal end (c).

that the arterial shape is implicitly represented on a Cartesian grid, with a cell size of 1 mm, using the SDF function, and thus the arterial thickness is not explicitly determined. The SDF was calculated using the open-source software V-SDFlib [44].

Figure 3 shows the procedure of deploying the braided stent into arteries. First, the stent is placed in the straight catheter tube with a diameter of 5 mm and compressed in the radial direction as it approaches a catheter diameter of 0.7 mm (Fig. 3(a)). Second, the catheter and the stent inside the catheter are deformed to fit the centerline of curved arteries (Fig. 3(b)). Third, the stent is deployed by pulling the catheter from the distal to the proximal side (Fig. 3(c)). Note that both ends of the braided stent are free and the whole process is performed in a quasi-static manner.

3 | RESULTS

3.1 | Stent shape transition during deployment

Figure 4 (a) shows representative snapshots of the process of deploying the braided stent from the catheter into the straight artery. The stent self-expands uniformly to the arterial wall from the distal to the proximal end, while there is incomplete expansion at both proximal and distal ends. The instantaneous stent diameter during deployment along the longitudinal axis of the artery is shown in Fig. 4 (b). Stent diameters approach the arterial diameter (4 mm) in the central domain, whereas the diameters of both ends are relatively small and approximately 25% lower at the proximal end. This local incomplete expansion, known as the fish-mouth phenomenon, is consistent with observations made in phantom experiments [9, 11].

Figure 5 shows representative snapshots of deploying the braided stent into curved arteries with low curvature (0.05 mm^{-1}) and high curvature (0.094 mm^{-1}), as representative cases. The stent is successfully expanded to fit the arterial wall except at both ends in the case of an artery with low curvature and in the case of a straight artery (Fig. 4). Although these tendencies are also observed in other cases with different curvatures, the stent becomes flattened at the midsection of the artery during deployment in the case of high curvature (0.094 mm^{-1}).

For quantitative evaluation of the stent shape after deployment, we define the flatness ratio of the stent cross-section ϕ as an evaluation index. The stent cross section is approximated as an ellipsoid using a gyration tensor

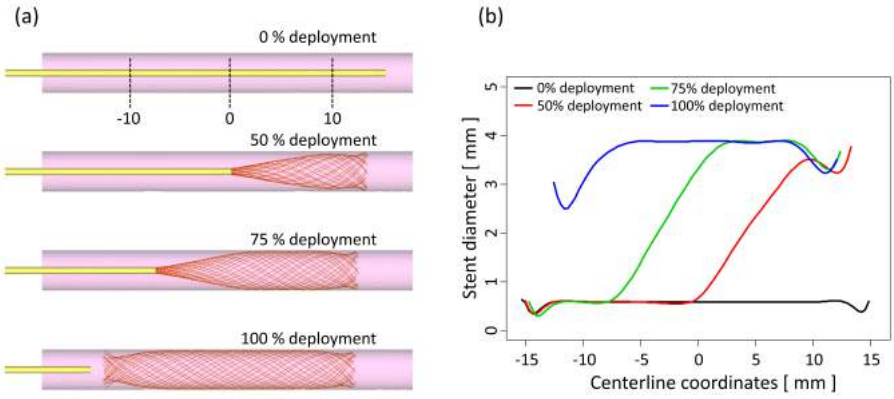

FIGURE 4 Snapshots of stent deployment into a straight artery (a) and spatial distributions of the instantaneous stent diameter along arterial centerlines (z-axis) at (b) 0% deployment (i.e., before deployment), 50% deployment, 75% deployment, and 100% deployment (i.e., after deployment).

$\mathbf{S} \in \mathbb{R}^{2\times 2}$ in the cross-sectional plane. Its components S_{ij} are defined as

$$S_{ij} = \frac{1}{N}\sum_{k=1}^{N} x_i^k x_j^k, \tag{10}$$

where $\mathbf{x}$ is the position vector of stent wires in the cross-sectional plane and N is the number of stent wires. Lengths of longer and shorter axes of the ellipsoid, a and b, can be calculated from the eigenvalues and corresponding eigenvectors of $\mathbf{S}$. Using a and b, the flatness ratio of the ellipsoid $\phi (0 \le \phi \le 1)$ is given by

$$\phi = \left|\frac{a-b}{a+b}\right|. \tag{11}$$

The stent shape is a circle when $\phi = 0$ and completely flattened when $\phi = 1$. Figure 6 shows the spatial distribution of the flatness ratio of the stent ϕ after deployment in all cases. The flatness ratio is almost zero in the case of a straight artery and lower than 0.2 in cases that the curvature is lower than 0.076 mm^{-1}. For curvature of 0.087 mm^{-1}, the flatness ratio is higher than that in cases of lower curvature and higher than 0.2 at the proximal ends. For curvature of 0.094 mm^{-1}, the flatness ratio becomes dramatically high in the proximal domain (s < 0) and approaches 0.8.

3.2 | Mechanical energy transition during deployment

To interpret behaviors of the braided stent during deployment from a mechanical viewpoint, we evaluate the transition of mechanical energy stored in stent wires during deployment. Figure 7 shows transitions of total elastic energy U during stent deployment in all cases. The total elastic energy is almost the same at the beginning of deployment regardless of the arterial curvature and gradually decay during deployment process. However, the falling gradient becomes moderate with increasing arterial curvature, and the elastic energy in the case of the highest curvature (0.094 mm^{-1}) is more than twice that in the case of a straight artery.

Figure 8 shows transitions of the stretching/compression, bending, and torsional energies during deployment into a straight artery and curved arteries with low curvatures (0.05 mm^{-1}) and high curvatures (0.094 mm^{-1}) as representa-

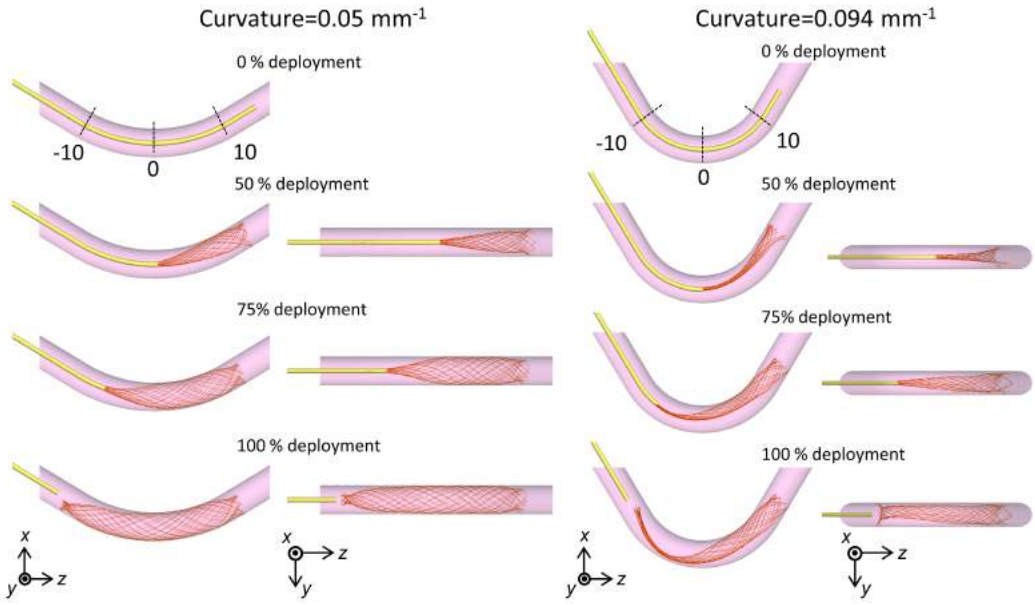

FIGURE 5 Snapshots of the braided stent deployment at 0% deployment (i.e., before deployment), 50% deployment, 75% deployment, and 100% deployment (i.e., after deployment) for arterial curvature of 0.05 mm^{-1} (left) and 0.094 mm^{-1} (right), as representative cases.

tive examples. In the case of a straight artery (Fig. 8(left)), the bending energy is dominantly stored in stent wires and the torsional energy is almost zero at the beginning of deployment (0% deployment). The bending energy is almost constant until 40% deployment whereas it then monotonically decreases until the end of deployment (100% deployment). The torsional energy gradually increases during the deployment process, whereas this increase disappears when the whole domain of the stent is released from the catheter. These tendencies are found in cases of low curvature (Fig. 8(center)). In the case of high curvature (Fig. 8(right)), the bending energy is relatively low at the beginning of deployment and remains constant until 50% deployment. Although it monotonically decreases with proceeding deployment, there are still high values of bending energy at the end of deployment. The torsional energy becomes high at the beginning of deployment and remains almost constant throughout the deployment process. Note that the stretching/compression energy is almost zero throughout the process in all cases.

To evaluate transitions of the spatial distribution of elastic energies, we divided the arterial interior into multiple sections of 0.5 mm along the centerline coordinates of the artery and computed the summation of elastic energies stored in the stent wires for each section. Figure 9 shows the spatial distribution of the mechanical energies stored in the stent along the centerline of the artery at 0%, 75%, and 100% deployment into straight and curved arteries with low (=0.05 mm^{-1}) and high curvatures (=0.094 mm^{-1}), as representative examples. In the case of the straight artery (Fig. 9(left)), the bending energy is nearly constant except at proximal and end domains, where the elastic energy is locally low. With proceeding deployment, the bending energy is released and approaches zero in released domains whereas it locally increases in the proximal domain where the stent is still compressed in the catheter. After deployment, almost all bending energy is released and there is nearly zero bending energy throughout the stent domain. The torsional energy is almost zero throughout the stent domain before and after deployment but there is a

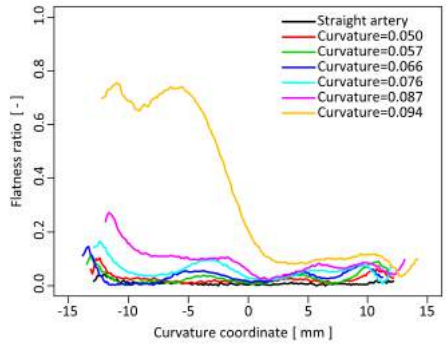

FIGURE 6 Spatial distribution of the flatness ratio of braided stent cross-sections after deployment along the centerline of arteries.

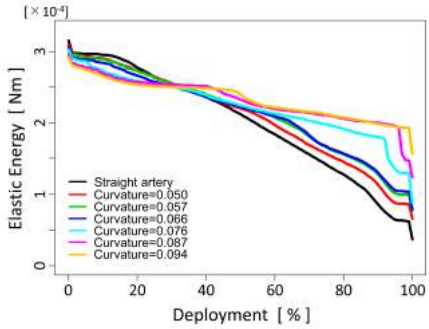

FIGURE 7 Transition of the mechanical energy of the braided stent during deployment in seven cases with different arterial curvatures.

local increase in the domain where just released during deployment. In the case of low curvature (Fig. 9(center)), the distribution of the bending energy has the same tendencies as in the case of the straight artery, whereas the torsional energy is locally high in the midsection of the arterial curve at the beginning of deployment. This local torsional energy is maintained during the deployment process but only slightly remains at the end of deployment. In the case of high curvature (Fig. 9(right)), the spatial distribution of the bending energy has the same tendencies as in other cases at the beginning of deployment. The extent of local release in the distal domain and the increase in the proximal domain are relatively small, and relatively high values remain after deployment. Relatively high torsional energy is found in the midsection of the artery at the beginning of deployment, and these values and the distribution remain almost constant throughout the deployment process.

Figure 10 visually compares the bending and torsional energies in each beam element during deployment into arteries with low curvature and high curvature. In the bending energy distribution, the bending energy is locally high around the catheter tip in all cases during deployment and released after deployment while relatively high energy remains in an unexpanded domain in the case of high curvature (Fig. 10(left)). In the torsional energy distribution, torsional energy is relatively high on the internal side of the curved artery and concentrates in the middle section of the curvature (Fig. 10(right)). These values and distribution have the same tendency in the deployment process.

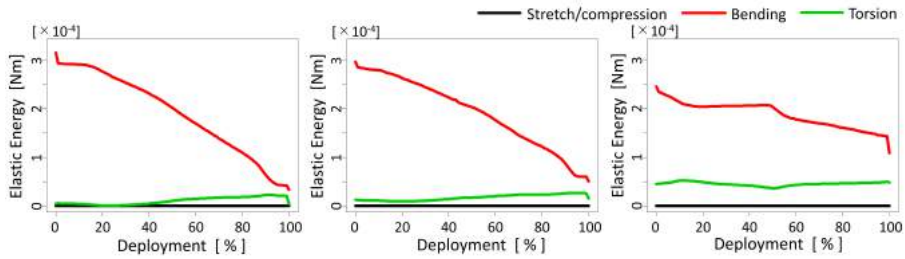

FIGURE 8 Transitions of the mechanical energy components (stretching/compression, bending, and torsional energies) stored in the braided stent during deployment into the straight artery (left) and curved arteries with curvature of 0.05 mm^{-1}(center) and 0.094 mm^{-1}(right).

4 | DISCUSSION

Much attention has been paid to the mechanical characteristics of the braided stent because of the stent's increasing clinical importance, and computational approaches have greatly contributed to clarifying apparent mechanical properties of the stent [18, 19, 20, 21, 22, 23, 24, 25]. Several numerical experiments that consider detailed mechanical characteristics of stent wires, such as the material nonlinearity [18, 20, 21, 24] and three-dimensional stress-field [21, 22, 25], have been conducted. The present study also conducted a computational mechanical analysis of the braided stent; however, the motivation and aim of the present study are different from those of existing computational studies. We simulated stent deployment in the present study to clarify mechanical behaviors during the deployment process and interpreted the underlying mechanism of the inappropriate stent expansion, especially the stent flattening phenomenon. To express the intuitive mechanical behaviors of the stent, we modeled the stent to be a set of wires, where the mechanical properties of the wires were simplified by introducing Kirchhoff's rod theory while the geometrical nonlinearity of wires including large deflection was precisely treated adopting the corotational beam element formulation described in [32, 33]. This sophisticated computational model allowed us to capture mechanically consistent stent behavior under idealized conditions. Using this model, we simulated the deployment of a stent into curved arteries with various curvatures and then presented the characteristic shape of the inappropriate stent expansion observed in clinical practice. This achievement successfully demonstrates that the computational mechanical model of the braided stent has great potential as a tool for interpreting the mechanism of a clinically problematic real phenomenon and apparent mechanical properties obtained in previous numerical experiments. Mechanical characteristics of inappropriate stent expansion observed from the obtained results are discussed below.

Stent flattening is a critical issue in clinical practice for the middle section of the arterial curve during deployment in cases of highly curved arteries, as observed by [8]. Characteristic shapes of stent flattening were observed in the present study in the case of high curvature (Fig. 6). To interpret this phenomenon from a mechanical viewpoint, the transition of mechanical energy stored in stent wires during deployment was evaluated. In cases of a straight catheter, the bending energy was stored in wires whereas longitudinal and torsional energy was almost zero. An increase in the arterial curvature decreased the bending energy but increased the torsional energy mainly on the inner side of the braided stent in the middle section of the arterial curve (Fig. 10). Stent flattening arose when there was higher torsional energy in the midsection of the arterial curve (Fig. 9). According to theoretical studies, radial forces of the braided stent for expansion originate from the bending energy stored in stent wires [14, 15, 16, 17]. The results therefore suggest that higher torsional energy functions to resist radial forces and release the bending energy and

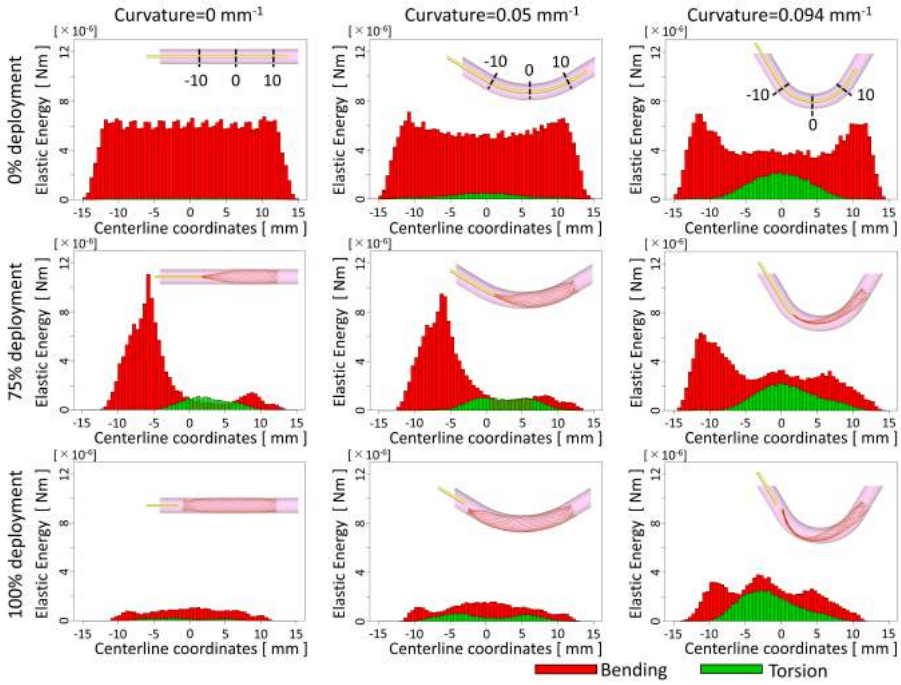

FIGURE 9 Spatial distributions of bending and torsional energy densities stored in the braided stent at 0% deployment (before deployment, top), 75% deployment (middle), and 100% deployment (after deployment, bottom). The arterial curvature is 0 mm^{-1} (left), 0.05 mm^{-1} (center), and 0.094 mm^{-1} (right). Red and green boxes respectively show bending, and torsional energy densities.

form the shape of the stent flattening in the mechanical equilibrium state. This suggestion explains that the stent flattening mechanism is a balancing of mechanical energy stored in stent wires.

In terms of clinical implication, the obtained results suggest that stent flattening could be avoided by keeping the bending energy stored in stent wires dominant during the deployment process. To achieve this, further considerations of the material properties of the stent wires and references state of the braided angle are potentially useful. For example, the braided angle is an essential factor in increasing the bending energy stored in stent wires, which was shown theoretically [14]. In fact, Valdivia y Alvarado et al. [11] reported that stent flattening was not observed in cases using a stent with a high braided angle. Furthermore, numerical optimization of the braided stent to reduce the use of stent wires while maintaining radial stiffness has been reported [19]. Adopting this strategy, two-objective optimization that maximizes/minimizes the bending/torsional energies stored in stent wires might provide a valuable solution to minimize the risk of the stent flattening.

Results of the present study show that both ends of the braided stent incompletely expanded regardless of arterial curvature (Fig. 4,5). These geometric characteristics have been reported and called the fish-mouth phenomenon in previous experimental observations [9]. Although the bending energy stored in stent wires may be essential to stent self-expansion (c.f., [14, 15, 16, 17]), the bending energy was relatively low in both end domains in the catheter (Fig. 9) because the stent ends were set to be free. These results suggest that the fish-mouth phenomenon results from the radial force being insufficient at both ends owing to the relatively low bending energy stored. Note that both ends of the braided stent used in clinical practice are flared and the wires are connected such that complete expansion

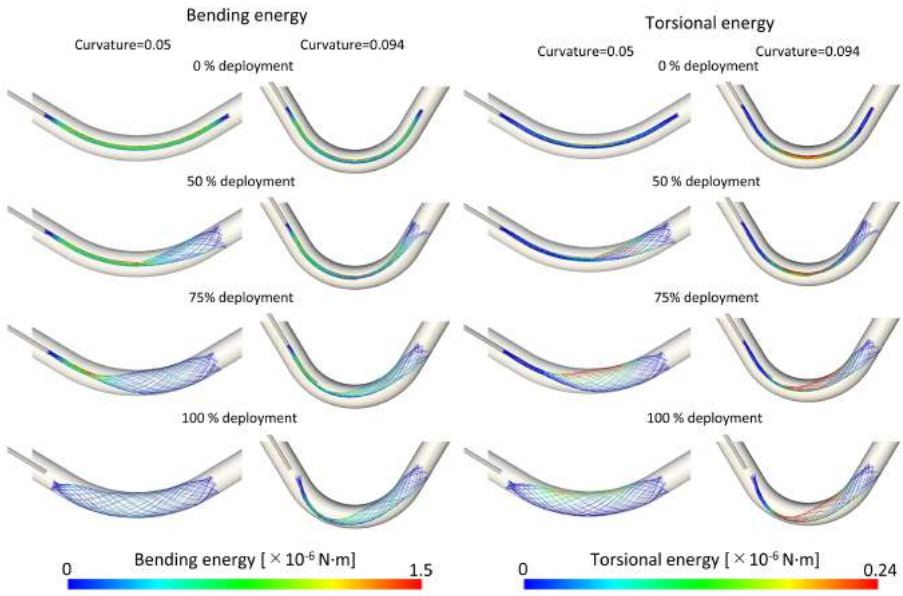

FIGURE 10 Spatial distributions of the bending energies (left) and torsional energies (right) in the braided stent at 0%, 50%, 75%, and 100% deployment in cases of low and high curvature.

is expected [20, 25]. The obtained results reveal that these designs can be considered to help increase the bending energy stored in the stent ends for complete expansion.

The present study has mainly four limitations. First, the stent mechanical modeling makes several assumptions that might affect the interpretation of the current results quantitatively. Stent wire mechanics were modeled using Kirchhoff's rod theory in eq. 1, and the material nonlinearity of stent wires [21, 24] was thus not considered. The deployment of a braided stent into a highly curved artery may cause mechanical instability owing to large deflection and geometrical and mechanical constraints due to multiple contacts, and such nonlinearity may affect the solution and make the quantitative evaluation from obtained results difficult. Second, we used relatively high values of the frictional coefficient comparing with existing studies determined from surface properties (c.f., [45]) to satisfy geometrical characteristics of the braided stent observed in our preliminary experiment. We conducted a preliminary experiment of braided stent deployment and confirmed that there was no clear sliding among adjacent wires even in the case that stent flattening was found. We therefore selected a coefficient of friction that avoided the sliding of adjacent stent wires although high friction may overly constrain wire motions. Techniques of expressing the contact condition of the braided stent are still under discussion even in cases of the braided stent being outside the catheter [29], and the equivalent friction coefficient of stent wires inside the catheter should thus be further considered. Third, the deployment conditions of the braided stent were idealized; e.g., the guidewire of the catheter was not considered, the catheter wall was assumed to be rigid, the catheter centerline was fixed on the arterial centerline, and stent deployment was represented by releasing the geometric constraint of the catheter wall while no other disturbances were loaded on the stent. These idealized conditions may also constraint the motion of the braided stent and thus lead to the overestimation of the risk of inappropriate stent expansion. Forth, this study simulated limited cases of stent deployment using the same stent model. Extensive parameter sensitivity analysis of the geometrical properties of the

braided stent would be useful in investigating to what extent the stent geometrical properties affect the mechanical energy transition and associated stent expansion properties.

5 | CONCLUSIONS

The present study developed a computational model of the braided stent that explicitly expresses mechanical behaviors of stent wires and performed numerical simulations of examples of braided stent deployment into arteries with various curvatures. In cases of low curvature, the braided stent successfully self-expands by releasing bending energy stored in wires in the catheter, whereas local incomplete expansion occurs at both ends where the bending energy is relatively low (i.e., the fish-mouth phenomenon). An increase in the arterial curvature increases the torsional energy stored in stent wires in the middle section of the arterial curve and stent flattening is observed when relatively high torsional energy is generated at the beginning of deployment. In this case, the bending energy in the stent wires is not fully released, and the torsional energy stored by high curvature may therefore resist the release of the bending energy and induce stent flattening. Obtained results suggest that the mechanical state of the braided stent in the catheter and the energy transition of the braided stent during deployment elucidate the underlying mechanism of the inappropriate expansion of the braided stent. This speculation highlights advantages of the computational mechanical modeling of the braided stent for better understanding of the intuitive mechanics of the stent associated with clinical issues.

acknowledgements

We thank Shotaro Tomotake, Taiki Shigematsu, and Naoki Takeishi for fruitful discussions. We thank Glenn Pennycook, MSc, from Edanz Group (www.edanzediting.com/ac) for editing a draft of this manuscript. This work was supported by research grants from JSPS Grants-in-Aid for Early-Career Scientists (18H18367 to Otani) and MEXT as "Priority Issue on Post-K computer(Supercomputer Fugaku)" (Integrated Computational Life Science to Support Personalized and Preventive Medicine)(hp190187 to Wada).

conflict of interest

The authors have no financial or personal interests in the work reported in this paper.

references

[1] Kis B, Weber W, Berlit P, Kühne D. Elective Treatment of Saccular and Broad-necked Intracranial Aneurysms using a Closed-cell Nitinol Stent (Leo). Neurosurgery 2006 mar;58(3):443–450.

[2] Piotin M, Blanc R, Spelle L, Mounayer C, Piantino R, Schmidt PJ, et al. Stent-Assisted Coiling of Intracranial Aneurysms. Stroke 2009;41(1):110–115.

[3] Nelson PK, Lylyk P, Szikora I, Wetzel SG, Wanke I, Fiorella D. The pipeline embolization device for the intracranial treatment of aneurysms trial. American Journal of Neuroradiology 2011;32(1):34–40.

[4] Brinjikji W, Murad MH, Lanzino G, Cloft HJ, Kallmes DF. Endovascular treatment of intracranial aneurysms with flow diverters: A meta-analysis. Stroke 2013;44(2):442–447.

[5] Becske T, Kallmes DF, Saatci I, McDougall CG, Szikora I, Lanzino G, et al. Pipeline for Uncoilable or Failed Aneurysms: Results from a Multicenter Clinical Trial. Radiology 2013;267(3):858–868.

[6] Lubicz B, Collignon L, Raphaeli G, Pruvo JP, Bruneau M, De Witte O, et al. Flow-diverter stent for the endovascular treatment of intracranial aneurysms: A prospective study in 29 patients with 34 aneurysms. Stroke 2010;41(10):2247–2253.

[7] Mintz GS. What to Do About Late Incomplete Stent Apposition? Circulation 2007;115(18):2379–2381.

[8] Krischek Ö, Miloslavski E, Fischer S, Shrivastava S, Henkes H. A comparison of functional and physical properties of self-expanding intracranial stents. Minimally Invasive Neurosurgery 2011;54(1):21–28.

[9] Ebrahimi N, Claus B, Lee CY, Biondi A, Benndorf G. Stent conformity in curved vascular models with simulated aneurysm weeks using Flat-Panel CT: An in vitro study. American Journal of Neuroradiology 2007;28(5):823–829.

[10] Szikora I, Berentei Z, Kulcsar Z, Marosfoi M, Vajda ZS, Lee W, et al. Treatment of intracranial aneurysms by functional reconstruction of the parent artery: The Budapest experience with the pipeline embolization device. American Journal of Neuroradiology 2010;31(6):1139–1147.

[11] Valdivia y Alvarado M, Ebrahimi N, Benndorf G. Study of conformability of the new LEO PLUS stent to a curved vascular model using flat-panel detector computed tomography (DynaCT). Neurosurgery 2009;64(3 SUPPL.):130–134.

[12] Aurboonyawat T, Blanc R, Schmidt P, Piotin M, Spelle L, Nakib A, et al. An in vitro study of silk stent morphology. Neuroradiology 2011;53(9):659–667.

[13] Shapiro M, Raz E, Becske T, Nelson PK. Variable porosity of the pipeline embolization device in straight and curved vessels: A guide for optimal deployment strategy. American Journal of Neuroradiology 2014;35(4):727–733.

[14] Jedwab MR, Clerc CO. A study of the geometrical and mechanical properties of a self-expanding metallic stent–theory and experiment. Journal of applied biomaterials 1993;4(1):77–85.

[15] Wang R, Ravi-Chandar K. Mechanical Response of a Metallic Aortic Stent—Part I: Pressure-Diameter Relationship. Journal of Applied Mechanics 2004;71(5):697.

[16] Wang R, Ravi-Chandar K. Mechanical Response of a Metallic Aortic Stent—Part II: A Beam-on-Elastic Foundation Model. Journal of Applied Mechanics 2004;71(5):706.

[17] Moon T, Hong D, Chun HJ, Lee KB. Analytical models for predicting mechanical properties of mesh-type self-expandable metal stents with cover membrane. Current Applied Physics 2009;9(1):92–100.

[18] Kim JH, Kang TJ, Yu WR. Mechanical modeling of self-expandable stent fabricated using braiding technology. Journal of Biomechanics 2008;41(15):3202–3212.

[19] De Beule M, Van Cauter S, Mortier P, Van Loo D, Van Impe R, Verdonck P, et al. Virtual optimization of self-expandable braided wire stents. Medical Engineering and Physics 2009;31(4):448–453.

[20] Zhao S, Liu XC, Gu L. The Impact of Wire Stent Fabrication Technique on the Performance of Stent Placement. Journal of Medical Devices 2012;6(1):011007.

[21] Frost M, Sedlák P, Kruisová A, Landa M. Simulations of self-expanding braided stent using macroscopic model of NiTi shape memory alloys covering R-Phase. Journal of Materials Engineering and Performance 2014;23(7):2584–2590.

[22] Ni XY, Pan CW, Gangadhara Prusty B. Numerical investigations of the mechanical properties of a braided non-vascular stent design using finite element method. Computer Methods in Biomechanics and Biomedical Engineering 2015;18(10):1117–1125.

[23] Alherz AI, Tanweer O, Flamini V. A numerical framework for the mechanical analysis of dual-layer stents in intracranial aneurysm treatment. Journal of Biomechanics 2016;49(12):2420–2427.

[24] Shanahan C, Tofail SAM, Tiernan P. Viscoelastic braided stent: Finite element modelling and validation of crimping behaviour. Materials and Design 2017;121:143–153.

[25] Ni XY, Zhang YH, Zhao HX, Pan CW. Numerical research on the biomechanical behaviour of braided stents with different end shapes and stent-oesophagus interaction. International Journal for Numerical Methods in Biomedical Engineering 2018;34(6):1–16.

[26] Fu W, Cheng G, Yan R, Qiao A. Numerical investigations of the flexibility of intravascular braided stent. Journal of Mechanics in Medicine and Biology 2017;17(4):1750075.

[27] Fu W, Xia Q, Yan R, Qiao A. Numerical investigations of the mechanical properties of braided vascular stents. Bio-Medical Materials and Engineering 2018;29(1):81–94.

[28] Suzuki T, Takao H, Fujimura S, Dahmani C, Ishibashi T, Mamori H, et al. Relationships between geometrical parameters and mechanical properties for a helical braided flow diverter stent. Technology and Health Care 2017 aug;25(4):611–623.

[29] Kelly N, McGrath DJ, Sweeney CA, Kurtenbach K, Grogan JA, Jockenhoevel S, et al. Comparison of computational modelling techniques for braided stent analysis. Computer Methods in Biomechanics and Biomedical Engineering 2019;22(16):1334–1344.

[30] Dill EH. Kirchhoff's Theory of Rods. Archives for History of Exact Sciences 1992;44(1):1–23.

[31] Stoop N, Najafi J, Wittel FK, Habibi M, Herrmann HJ. Packing of Elastic Wires in Spherical Cavities. Physical Review Letters 2011 may;106(21):214102.

[32] Pacoste C, Eriksson A. Beam elements in instability problems. Computer Methods in Applied Mechanics and Engineering 1997;144(1-2):163–197.

[33] Battini JM, Pacoste CJ. Co-rotational beam elements with warping effects in instability problems. Computer Methods in Applied Mechanics and Engineering 2002;191:1755–1789.

[34] Otani T, Wada S, Tanaka M. Modeling of endovascular coiling to cerebral aneurysms: Effects of friction on coil mechanical behaviors. International Journal of Mechanical Sciences 2020;166:105206.

[35] Otani T, Shindo T, Ii S, Hirata M, Wada S. Effect of local coil density on blood flow stagnation in densely coiled cerebral aneurysms: a computational study using a Cartesian grid method. Journal of Biomechanical Engineering 2018;140:041013.

[36] Munjiza A, Andrews K. NBS contact detection algorithm for bodies of similar size. International Jounral for Numerical Methods in Engineering 1998;149:131–149.

[37] Wriggers P, Zavarise G. On contact between three-dimensional beams undergoing large deflections. Communications in Numerical Methods in Engineering 1997;13:429–438.

[38] Mishra B, Rajamani R. The discrete element method for the simulation of ball mills. Applied Mathematical Modelling 1992;16(April):598–604.

[39] Margolis D. Fixed causality slip-stick friction models for use in simulation of non-linear systems. In: Proceedings of the Institution of Mechanical Engineers. Part I: Journal of Systems and Control Engineering, vol. 219; 2005. p. 199–206.

[40] Vetter R. Growth, Interaction and Packing of Thin Objects. PhD thesis, Eidgenössische Technische Hochschule Zürich; 2015.

[41] Vetter R, Wittel FK, Stoop N, Herrmann HJ. Finite element simulation of dense wire packings. European Journal of Mechanics / A Solids 2013;37:160–171.

[42] Zienkiewicz OC, Xie M Y. A simple error estimator and adaptive time stepping procedure for dynamic analysis. Earthquake Engineering & Structural Dynamics 1991;20:871–887.

[43] Zeng LF, Wiberg NE, Li XD, Xie YM. A posteriori local error estimation and adaptive time-stepping for newmark integration in dynamic analysis. Earthquake Engineering & Structural Dynamics 1992 jan;21(7):555–571.

[44] V-SDFlib;. https://vcad-hpsv.riken.jp/en/release_software/VSDFlib/.

[45] Ma D, Dumont TM, Kosukegawa H, Ohta M, Yang X, Siddiqui AH, et al. High fidelity virtual stenting (HiFiVS) for intracranial aneurysm flow diversion: In vitro and in silico. Annals of Biomedical Engineering 2013;41(10):2143–2156.